

RESEARCH ARTICLE

A Hybrid Multiscale Model of Miscible Reactive Fronts

10.1002/2017WR020867

Natalia Siuliukina¹ and Daniel M. Tartakovsky² 

Key Points:

- Highly localized reactive fronts defy a Darcy-scale description
- Hybrid models of dynamic reactive fronts combine pore- and Darcy-scale models
- Hybrids capture miscible front dynamics at a fraction of the pore-scale simulations

Correspondence to:

D. Tartakovsky,
tartakovsky@stanford.edu

Citation:

Siuliukina, N., & Tartakovsky, D. M. (2018). A hybrid multiscale model of miscible reactive fronts. *Water Resources Research*, 54, 61–71. <https://doi.org/10.1002/2017WR020867>

Received 31 MAR 2017

Accepted 9 DEC 2017

Accepted article online 14 DEC 2017

Published online 5 JAN 2018

¹Department of Mechanical and Aerospace Engineering, University of California, San Diego, La Jolla, CA, USA,

²Department of Energy Resources Engineering, Stanford University, Stanford, CA, USA

Abstract Subsurface processes can be simulated at multiple scales with variable degrees of fidelity. Some microscopic (pore-scale) features of reactive transport cannot be properly resolved in macroscopic (Darcy-scale) models. While microscopic descriptors might be closer to reality, they are computationally unfeasible when deployed on a macroscale. Hybrid algorithms combine the physical fidelity of a microscopic model with the computational efficiency of its macroscopic counterpart. We develop a hybrid model of dynamic reactive fronts in an open fracture, with a chemical reaction occurring in the zone of contact between two dissolved species. Away from the front, both fluid flow and solute transport are described by one-dimensional models. In the front's proximity, two-dimensional Stokes equations are used to model fluid flow, and solute transport is described with advection-diffusion-reaction equations. These two descriptors are coupled via an iterative procedure, which enforces the continuity of concentrations and mass fluxes across the interface between the two models. Our numerical experiments demonstrate that the hybrid model outperforms its microscopic and macroscopic counterparts in terms of computational time and representational accuracy, respectively.

1. Introduction

Reaction fronts moving with a fluid are a characteristic feature of many physical, chemical, and biological processes (e.g., Coveney & Fowler, 2005; De Wit, 2004; Fernandez & Homsy, 2003; Johnson et al., 1985). This phenomenon occurs when a fluid with a dissolved species *A* displaces a fluid (the same or different) with a dissolved species *B*. A chemical reaction, e.g., $A+B \rightarrow C$, occurs within a spatially localized region (a "front") separating these two solutions. The position and width of this front change with time due to fluid flow, molecular diffusion, and hydrodynamic dispersion. While localized reaction fronts might occupy a minuscule fraction of a flow domain, their effects on flow and transport can be felt over much larger regions (Gálfi & Rácz, 1988).

Like all subsurface flow and transport processes, dynamic reaction fronts can be described with either pore-scale (microscopic) or Darcy-scale (macroscopic) models. The former have a solid physical foundation consisting of Stokes equations for flow and advection-reaction-diffusion equations for transport; yet they are impractical for large-scale simulations of practical interest because of the lack of knowledge about pore geometry and prohibitively high computational cost. A set of simplifying assumptions is required to derive equations for average flow velocity (Darcy's law) and solute concentration (advection-dispersion equation or ADE), which provide Darcy-scale descriptors of flow and transport in porous media. Such macroscopic models fail when some of these assumptions become invalid (Battiato & Tartakovsky, 2011; Battiato et al., 2009; Boso & Battiato, 2013). If the failure of macroscopic models is confined to a small region of a computational domain, hybrid pore-scale/Darcy-scale algorithms (e.g., Tartakovsky et al., 2008) allow one to combine the high fidelity of microscopic models with the computational efficiency of their macroscopic counterparts. Hybrid algorithms yield accurate predictions, while keeping computational cost relatively low by restricting microscopic simulations to subdomains wherein macroscopic models break down, and solving macroscopic equations in the rest of the computational domain (e.g., Alexander et al., 2002, 2005a, 2005b; Taverniers et al., 2014). Hybrid algorithms for subsurface applications have been developed by Battiato et al. (2011), Roubinet and Tartakovsky (2013), Balhoff et al. (2008), Tomin and Lunati (2013), and Tang et al. (2015). In these and other similar analyses, the microscopic and macroscopic simulation domains are fixed in space.

A major goal of our analysis is to develop a hybrid model of dynamic reactive fronts, which involve two dissolved species undergoing a nonlinear homogeneous reaction to produce another solute. A set of numerical

experiments is performed to investigate the validity of the homogenizability conditions for multicomponent reactive flow in a horizontal open fracture. When these conditions are not met, we deploy the hybrid algorithm that couples a pore-scale model in the vicinity of a moving reaction front with a corresponding Darcy-scale model elsewhere in the fracture. The two models are coupled via an iterative procedure, which enforces the continuity of concentrations and mass fluxes across the interface between the two models.

Section 2 contains pore- and Darcy-scale formulations of flow and reactive transport in both general porous media and an open fracture; it also summarizes, in the form of a phase diagram in the space of Péclet and Damköhler numbers, the conditions under which the Darcy-scale model becomes invalid. In section 3, we develop our hybrid algorithm for dynamic reactive fronts. In section 4, we report results of our numerical experiments in various transport regimes, including those under which the Darcy-scale model becomes invalid and either the pore-scale model or the hybrid must be used. The relative performance of the three modeling strategies is compared in terms of both accuracy and computational time. Main conclusions drawn from our study are presented in section 5.

2. Problem Formulation

We consider both pore-scale and Darcy-scale descriptions of fluid flow and reactive solute transport in a generic porous medium $\hat{\Omega}$. The material's pore space, denoted by $\hat{\mathfrak{R}} \subset \hat{\Omega}$, is fully saturated with a fluid of dynamic viscosity μ . The (multiconnected) solid-fluid interface is denoted by $\hat{\Gamma}$. The fluid is a dilute solution of two chemical species A and B , which undergo an irreversible fast bimolecular reaction,



to form the reaction product C with the homogeneous reaction rate constant k [L/T]. We assume that this chemical reaction does not alter the pore space $\hat{\mathfrak{R}}$ and, hence, does not affect the flow velocity.

The pore-scale molar concentrations of the dissolved species A , B , and C are denoted by \hat{c}_i [M/L^3], where $i = A, B$, and C , respectively. The corresponding Darcy-scale concentrations \hat{C}_i [M/L^3] are averages of \hat{c}_i over a representative elementary volume $\hat{\mathcal{V}} \subset \hat{\Omega}$ centered around a point \mathbf{x} ,

$$\hat{C}_i(\mathbf{x}, t) = \frac{1}{|\hat{\mathcal{V}}|} \int_{\hat{\mathcal{V}}(\mathbf{x})} \hat{c}_i(\mathbf{y}, t) d\mathbf{y}, \quad i = A, B, C. \quad (2)$$

A characteristic length of $\hat{\mathcal{V}}$, ℓ , is much smaller than that of $\hat{\Omega}$, $\ell \ll L$, so that $\varepsilon \equiv \ell/L \ll 1$. Equations describing the spatiotemporal evolution of $\hat{c}_i(\hat{\mathbf{x}}, \hat{t})$ and $\hat{C}_i(\hat{\mathbf{x}}, \hat{t})$ are described below.

2.1. Pore-Scale Equations

Steady-state pressure-driven single-phase incompressible fluid flow is described by Stokes and continuity equations,

$$\mu \hat{\nabla}^2 \hat{\mathbf{v}} - \hat{\nabla} \hat{p} = \mathbf{0}, \quad \hat{\nabla} \cdot \hat{\mathbf{v}} = 0, \quad \hat{\mathbf{x}} \in \hat{\mathfrak{R}}, \quad (3)$$

where $\hat{\mathbf{v}}(\hat{\mathbf{x}})$ is the fluid velocity, $\hat{p}(\hat{\mathbf{x}})$ is the fluid pressure, and $\hat{\mathbf{x}}$ is a point in $\hat{\mathfrak{R}}$. Flow equations (3) are subject to no-slip boundary conditions on the impermeable solid-fluid interface $\hat{\Gamma}$, i.e., $\hat{\mathbf{v}} = \mathbf{0}$ for $\hat{\mathbf{x}} \in \hat{\Gamma}$.

The pore-scale concentrations $\hat{c}_i(\hat{\mathbf{x}}, \hat{t})$ are described by a system of coupled advection-diffusion-reaction equations,

$$\frac{\partial \hat{c}_i}{\partial \hat{t}} + \hat{\nabla} \cdot (\hat{\mathbf{v}} \hat{c}_i) = D \hat{\nabla}^2 \hat{c}_i - k \hat{c}_A \hat{c}_B, \quad i = A, B; \quad \hat{\mathbf{x}} \in \hat{\mathfrak{R}}, \quad \hat{t} > 0, \quad (4a)$$

and

$$\frac{\partial \hat{c}_C}{\partial \hat{t}} + \hat{\nabla} \cdot (\hat{\mathbf{v}} \hat{c}_C) = D \hat{\nabla}^2 \hat{c}_C + k \hat{c}_A \hat{c}_B, \quad \hat{\mathbf{x}} \in \hat{\mathfrak{R}}, \quad \hat{t} > 0. \quad (4b)$$

Here for the sake of simplicity and without loss of generality, we assume that the three dissolved species have the same molecular diffusion coefficient D [L^2/T]. Transport equations (4) are subject to no-flux boundary conditions on the solid-fluid interface $\hat{\Gamma}$ with unit normal vector $\hat{\mathbf{n}}(\hat{\mathbf{x}})$,

$$\hat{\mathbf{n}} \cdot \nabla \hat{c}_i = 0, \quad i = A, B, C; \quad \hat{\mathbf{x}} \in \hat{\Gamma}. \quad (5a)$$

and initial conditions

$$\hat{c}_i(\hat{\mathbf{x}}, 0) = \hat{c}_{in,i}, \quad i = A, B, C; \quad \hat{\mathbf{x}} \in \hat{\mathfrak{R}}, \quad (5b)$$

where $\hat{c}_{in,i}(\hat{\mathbf{x}})$ are known (possibly spatially varying) initial concentrations.

2.1.1. Dimensionless Formulation

Let L and v denote characteristic length and characteristic velocity magnitude, respectively; and set $c^* = \max\{\hat{c}_{in,A}, \hat{c}_{in,B}\}$. We introduce dimensionless parameters and independent and dependent variables,

$$Pe = \frac{vL}{D}, \quad Da = \frac{L^2 kc^*}{D}, \quad \mathbf{x} = \frac{\hat{\mathbf{x}}}{L}, \quad t = \frac{\hat{t}D}{L^2}, \quad \mathbf{v} = \frac{\hat{\mathbf{v}}}{v}, \quad p = \frac{\hat{p}L^2}{\mu v L}, \quad c_i = \frac{\hat{c}_i}{c^*}. \quad (6)$$

The Péclet number $Pe = t_d/t_a$ represents the ratio between the diffusion ($t_d = L^2/D$) and advection ($t_a = L/v$) time scales, while the Damköhler number $Da = t_d/t_r$ is defined as the ratio between the diffusion and reaction ($t_r = 1/kc^*$) time scales. (This scaling of pressure \hat{p} ensures that the rescaled viscous term has the same order of magnitude as its counterpart in the original Stokes equations.) Rewriting (3) and (4) in terms of the dimensionless quantities (6) yields a dimensionless form of the governing equations

$$\varepsilon^2 \nabla^2 \mathbf{v} - \nabla p = \mathbf{0}, \quad \nabla \cdot \mathbf{v} = 0, \quad \mathbf{x} \in \mathfrak{R}; \quad (7)$$

and

$$\frac{\partial c_i}{\partial t} + Pe \nabla \cdot (\mathbf{v} c_i) = \nabla^2 c_i - Da c_A c_B, \quad i = A, B; \quad \mathbf{x} \in \mathfrak{R}, \quad t > 0, \quad (8a)$$

$$\frac{\partial c_C}{\partial t} + Pe \nabla \cdot (\mathbf{v} c_C) = \nabla^2 c_C + Da c_A c_B, \quad \mathbf{x} \in \mathfrak{R}, \quad t > 0, \quad (8b)$$

subject to the correspondingly rescaled initial and boundary conditions.

2.2. Darcy-Scale Equations

Under certain conditions on Pe and Da , the spatial averaging of pore-scale equations (7) and (8) yields Darcy-scale (advection-dispersion-reaction) equations for the dimensionless macroscopic concentrations $C_i = \hat{C}_i/c^*$,

$$\frac{\partial C_i}{\partial t} + Pe \nabla \cdot (\mathbf{V} C_i) = \nabla \cdot (\mathbf{D} \nabla C_i) - Da C_A C_B, \quad i = A, B; \quad \mathbf{x} \in \Omega, \quad t > 0, \quad (9a)$$

and

$$\frac{\partial C_C}{\partial t} + Pe \nabla \cdot (\mathbf{V} C_C) = \nabla \cdot (\mathbf{D} \nabla C_C) + Da C_A C_B. \quad (9b)$$

Here $\mathbf{V}(\mathbf{x})$ is the Darcy flux (macroscopic velocity) computed by solving the groundwater flow equation, and $\mathbf{D}(\mathbf{U})$ is the dispersion coefficient tensor. Specifically, equations (9) are valid if (Boso & Battiato, 2013)

$$\varepsilon \ll 1, \quad Pe < \varepsilon^{-2}, \quad Da < \varepsilon^{-2}, \quad Da/Pe < \varepsilon^{-1}. \quad (10)$$

The inequality $\varepsilon \ll 1$ is a condition that ensures spatial-scale separation, $Pe < \varepsilon^{-2}$ ensures that the system is not dominated by advection at the microscale, $Da < \varepsilon^{-2}$ is the sufficient condition for good mixing of the reactants, and the condition $Da/Pe < \varepsilon^{-1}$ imposes a constraint on the advective and reactive time scales. These sufficient conditions delineate a homogenizability region in a two-dimensional Pe-Da space (Figure 1), where equations (9) are valid. The validity is guaranteed inside the region and not guaranteed outside.

Dynamic reactive fronts provide a challenging illustration of the possible breakdown of Darcy-scale models. Let us suppose that, at time

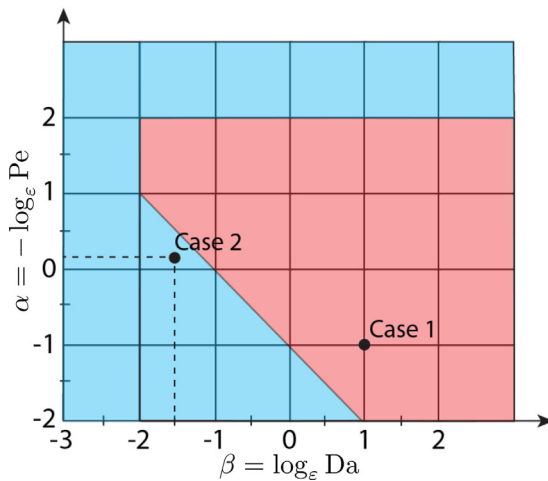


Figure 1. Region of the validity of the Darcy-scale transport model (9) in the Pe-Da phase space spanned by the Péclet (Pe) and Damköhler (Da) numbers. Case 1, $(\alpha, \beta) = (-1, 1)$, satisfies and Case 2, $(\alpha, \beta) = (1/4, -3/2)$, violates the homogenizability conditions (10).

$t = 0$, the solutes A and B occupy distinct subdomains Ω_A and Ω_B ($\Omega = \Omega_A \cup \Omega_B$), which are separated by an interface $\gamma = \Omega_A \cap \Omega_B$. This situation translates into (dimensionless) initial concentrations

$$c_{in,A} = \begin{cases} 1 & \mathbf{x} \in \Omega_A \\ 0 & \mathbf{x} \in \Omega_B \end{cases} \quad \text{and} \quad c_{in,B} = \begin{cases} 0 & \mathbf{x} \in \Omega_A \\ 1 & \mathbf{x} \in \Omega_B \end{cases}. \quad (11)$$

The reaction $A+B \rightarrow C$ takes place only in the immediate vicinity of the interface γ , which is both advected with the flow, $\gamma = \gamma(\mathbf{x}, t)$, and diffuses due to hydrodynamic dispersion. High concentration gradients in this diffuse reactive front can invalidate some of the homogenizability conditions (10), leading to a local breakdown of the Darcy-scale transport model (9). Our study has three interconnected objectives. First, we identify flow and transport regimes in which the breakdown indeed occurs, as predicted by the theory (Boso & Battiato, 2013). Second, we demonstrate that under these conditions, no amount of mesh refinement around the front, used to numerically solve (9), can remedy the model's inadequacy. Third, we show that the hybrid model outperforms its microscopic and macroscopic counterparts in terms of computational time and representational accuracy, respectively. These objectives are achieved via numerical experimentation with diffusive reactive fronts propagating through an open fracture.

2.3. Pore- and Darcy-Scale Models of Front Propagation in Fractures

Consider an open fracture of length L and width $2w$, such that $\hat{\Omega} = \{\hat{\mathbf{x}} = (\hat{x}, \hat{y})^T : 0 < \hat{x} < L, -w < \hat{y} < w\}$. Flow is driven by the externally imposed pressure gradient, $-J$ imposed in the \hat{x} direction.

2.3.1. Pore-Scale Model

Making use of the dimensionless quantities (6) and neglecting the boundary effects close to the fracture's entrance and exit, the solution of (7) in the rescaled fracture domain $\Omega = \{\mathbf{x} = (x, y)^T : 0 < x < 1, -\varepsilon < y < \varepsilon\}$ is given by Poiseuille's formula $\mathbf{v} = (u, 0)^T$ with

$$u(y) = \frac{3}{2} \left(1 - \frac{y^2}{\varepsilon^2} \right), \quad \varepsilon \equiv w/L. \quad (12)$$

(A dimensional form of Poiseuille's law obtained by solving [3] reads $\hat{u}(y) = J\varepsilon^2(1 - y^2/\varepsilon^2)/(2\mu)$. The average (characteristic) flow velocity is $v = (2\varepsilon)^{-1} \int_{-\varepsilon}^{\varepsilon} \hat{u}(y) dy = J\varepsilon^2/(3\mu)$. The definition of the dimensionless velocity in (6), $u = \hat{u}/v$, gives (12).) Pore-scale transport equations (8) reduce to

$$\frac{\partial c_i}{\partial t} + Pe u \frac{\partial c_i}{\partial x} = \frac{\partial^2 c_i}{\partial x^2} + \frac{\partial^2 c_i}{\partial y^2} - Da c_A c_B, \quad i = A, B; \quad \mathbf{x} \in \Omega, \quad t > 0, \quad (13a)$$

and

$$\frac{\partial c_C}{\partial t} + Pe u \frac{\partial c_C}{\partial x} = \frac{\partial^2 c_C}{\partial x^2} + \frac{\partial^2 c_C}{\partial y^2} + Da c_A c_B. \quad (13b)$$

Initial conditions leading to formation of a localized reactive front, (11), become

$$c_A(\mathbf{x}, 0) = \begin{cases} 1 & x \leq x_0 \\ 0 & x > 0 \end{cases}, \quad c_B(\mathbf{x}, 0) = \begin{cases} 0 & x \leq x_0 \\ 1 & x > 0 \end{cases}, \quad c_C(\mathbf{x}, 0) = \frac{1}{4}, \quad (14)$$

where x_0 is an initial position front $\gamma(t)$, and the initial value $c_C(\mathbf{x}, 0) = 1/4$ is arbitrarily selected for illustration purposes. Boundary conditions at the fractures' inlet and outlet are

$$c_A(0, y, t) = 1, \quad c_A(1, y, t) = 0, \quad |y| < \varepsilon, \quad t > 0; \quad (15a)$$

$$c_B(1, y, t) = 0, \quad c_B(0, y, t) = 1, \quad |y| < \varepsilon, \quad t > 0; \quad (15b)$$

$$c_C(0, y, t) = \frac{1}{4}, \quad c_C(1, y, t) = \frac{1}{4}, \quad |y| < \varepsilon, \quad t > 0. \quad (15c)$$

Boundary conditions at the fracture's walls are

$$\frac{\partial c_i}{\partial y}(x, \pm\varepsilon, t) = 0, \quad i = A, B, C; \quad 0 < x < 1, \quad t > 0. \quad (16)$$

2.3.2. Darcy-Scale Model

The (dimensionless) Darcy-scale concentrations $C_i(x, t)$ satisfy transport equations (9), which for the problem under consideration reduce to

$$\frac{\partial C_i}{\partial t} + Pe \frac{\partial C_i}{\partial x} = D \frac{\partial^2 C_i}{\partial x^2} - Da C_A C_B, \quad i=A, B; \quad 0 < x < 1, \quad t > 0, \quad (17a)$$

and

$$\frac{\partial C_C}{\partial t} + Pe \frac{\partial C_C}{\partial x} = D \frac{\partial^2 C_C}{\partial x^2} + Da C_A C_B, \quad i=A, B; \quad 0 < x < 1, \quad t > 0. \quad (17b)$$

The dispersion coefficient is now given by $D=1+2\epsilon^2 Pe^2/105$ (Boso & Battiato, 2013). Equations (17) are subject to initial conditions

$$C_A(x, 0) = \begin{cases} 1 & x \leq x_0 \\ 0 & x > x_0 \end{cases}, \quad C_B(x, 0) = \begin{cases} 0 & x \leq x_0 \\ 1 & x > x_0 \end{cases}, \quad C_C(x, 0) = \frac{1}{4}, \quad (18)$$

and boundary conditions

$$C_A(0, t) = 1, \quad C_A(1, t) = 0, \quad C_B(1, t) = 0, \quad C_B(0, t) = 1, \quad C_C(0, t) = \frac{1}{4}, \quad C_C(1, t) = \frac{1}{4}. \quad (19)$$

A solution of Darcy-scale model (14)–(17), $C_i(x, y, t)$ with $i=A, B$, and C , is consistent with its pore-scale counterpart (13)–(16), $c_i(x, y, t)$ with $i=A, B$, and C , if they satisfy the definition of Darcy-scale concentration (2),

$$\bar{c}_i(x, t) = \frac{1}{2\epsilon} \int_{-\epsilon}^{\epsilon} c_i(x, y, t) dy, \quad i=A, B, C; \quad (20)$$

i.e., if $C_i(x, t) = \bar{c}_i(x, t)$ for $i=A, B$, and C .

3. Hybrid Models of Dynamic Reactive Fronts

We present a general formulation of our hybrid model in section 3.1 and its implementation for transport in fractures in section 3.2.

3.1. General Hybrid Formulation

Let us suppose that, in the immediate neighborhood $\mathcal{N}_\delta[\gamma(\mathbf{x}, t)]$ of the reactive front's core $\gamma(\mathbf{x}, t)$, macroscopic equations (9) become invalid because some of the conditions in (10) are violated (see section 2.2). The dynamics of $\gamma(\mathbf{x}, t)$ is determined by advection, while the envelope $\partial\mathcal{N}_\delta(\mathbf{x}, t) = \gamma(\mathbf{x}, t) \pm \delta(\mathbf{x})$ represents the diffusive nature of dynamic reactive fronts. While the width of the reaction zone increases with time, we keep the width of $\mathcal{N}_\delta[\gamma(\mathbf{x}, t)]$ constant and set to $\delta \sim \sqrt{\|\mathbf{D}\|\Delta t}$ where Δt is a time step of the Darcy-scale simulations. That is because the concentration gradients in the outer edges of the diffuse reaction front are sufficiently small for the Darcy-scale model to be valid. The pore-scale model (7) and (8) is solved inside $\mathcal{N}_\delta[\gamma(\mathbf{x}, t)]$, and the Darcy-scale model (9) is solved elsewhere in the computational domain. The two models are coupled by enforcing the continuity of concentrations and the normal component of mass fluxes along the envelope $\partial\mathcal{N}_\delta$,

$$C_i(\mathbf{x}, t) = \frac{1}{\|\partial\mathcal{N}_\delta(\mathbf{x}, t)\|} \int_{\partial\mathcal{N}_\delta(\mathbf{x}, t)} c_i(s, t) ds, \quad J_i(\mathbf{x}, t) = \frac{1}{\|\partial\mathcal{N}_\delta(\mathbf{x}, t)\|} \int_{\partial\mathcal{N}_\delta(\mathbf{x}, t)} j_i(s, t) ds, \quad (21)$$

for $i=A, B$, and C . Here j_i and J_i are the normal components of the pore- and Darcy-scale dimensionless mass fluxes $\mathbf{j}_i = \mathbf{v}c_i - \nabla c_i$ and $\mathbf{J}_i = \mathbf{V}C_i - \mathbf{D}\nabla C_i$, respectively. The coordinate \mathbf{x} designates a segment of $\partial\mathcal{N}_\delta(\mathbf{x}, t)$ that falls within the corresponding element of a numerical mesh used in the Darcy-scale computation.

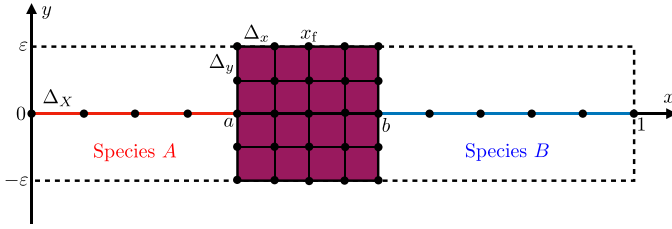


Figure 2. A dynamic diffused reaction front, centered at $x_f(t)$, propagating in an open fracture of dimensionless unit length and dimensionless width 2ε . Our hybrid algorithm solves the (two-dimensional) pore-scale model in the front's neighborhood $\mathcal{N}_\delta = \{\mathbf{x} : x_f(t) - a(t) < x < x_f(t) + b(t), -\varepsilon < y < \varepsilon\}$ and the (one-dimensional) Darcy-scale model in the rest of the fracture. The two models are coupled by enforcing the continuity conditions at $a(t)$ and $b(t)$.

3.2. Hybrid Model of Front Propagation in Fractures

The Darcy-scale description (14)–(17) reduces the front's core $\gamma(\mathbf{x}, t)$ to a single point $x_f(t)$. Starting with its initial position $x_f(0) = x_0$, the core propagates with dimensionless velocity Pe , so that $dx_f/dt = Pe$. The domain of pore-scale model (12)–(16) becomes $\mathcal{N}_\delta = \{\mathbf{x} : x_f(t) - \delta < x < x_f(t) + \delta, -\varepsilon < y < \varepsilon\}$ with the envelope consisting of two segments, $\partial\mathcal{N}_\delta = \{(x, y) : x_f(t) \pm \delta, -\varepsilon < y < \varepsilon\}$. Setting $\delta = m\sqrt{D\Delta t}$, these points are given by

$$a(t) = x_f(t) - m\sqrt{D\Delta t}, \quad b(t) = x_f(t) + m\sqrt{D\Delta t}, \quad (22)$$

where the coefficient m defines the dimensionless width of \mathcal{N}_δ (Figure 2). In the simulations reported below, we set $m = 2,800$, which corresponds to \mathcal{N}_δ occupying 20% of the whole simulation domain Ω .

The Darcy-scale model (14)–(17) is solved in the rest of the fracture $\mathcal{N}_\delta^c = \{x : 0 < x < a(t), b(t) < x < 1\}$. The continuity conditions (21) used to couple the pore- and Darcy-scale simulations take the form,

$$C_i(x, t) = \frac{1}{2\varepsilon} \int_{-\varepsilon}^{\varepsilon} c_i(y, t) dy, \quad J_i(x, t) = \frac{1}{2\varepsilon} \int_{-\varepsilon}^{\varepsilon} j_i(y, t) dy, \quad \text{for } x = a(t), b(t). \quad (23)$$

Our hybrid algorithm consists of the following steps.

1. Initiate simulations by setting $t = 0$ and $x_f(0) = x_0$; and by making an initial guess of the concentration values at $x = a$ and $x = b$, $C_{a,i}$ and $C_{b,i}$ with $i = A, B$, and C , respectively. (In the simulations reported below, we set $C_{a,A} = 0.8$, $C_{a,B} = 0.2$, $C_{a,C} = 0.5$, $C_{b,A} = 0.2$, $C_{b,B} = 0.8$, and $C_{b,C} = 0.5$.)

2. Compute $a(t)$ and $b(t)$ from (22), and assign pore- and Darcy-scale internal boundary conditions

$$c_i(a, y, t) = C_i(a, t) = C_{a,i}, \quad c_i(b, y, t) = C_i(b, t) = C_{b,i}, \quad i = A, B, C.$$

3. Solve the pore-scale equations (13) on domain $\mathcal{N}_\delta = \{x : a(t) < x < b(t), -\varepsilon < y < \varepsilon\}$. These equations are subject to initial and boundary conditions (14)–(16), which are supplemented with the interfacial conditions at $x = a(t)$ and $x = b(t)$ from step 2.

4. Solve the Darcy-scale equations (17) on domain $\mathcal{N}_\delta^c = \{x : 0 < x < a(t) \cup b(t) < x < 1\}$. These equations are subject to initial and boundary conditions (18) and (14), which are supplemented with the interfacial conditions at $x = a(t)$ and $x = b(t)$ from step 2.

5. Calculate pore-scale interfacial fluxes

$$j_i(x, y, t) = -\frac{\partial c_i}{\partial x}(x, y, t) + Pe u(y) c_{x,i}, \quad x = a, b, \quad i = A, B, C,$$

where $u(y)$ is given by (12) and $c_i(x, y, t)$ ($i = A, B$, and C) are computed in step 3. Evaluate average pore-scale interfacial fluxes

$$\bar{j}_i(x, t) = \frac{1}{2\varepsilon} \int_{-\varepsilon}^{\varepsilon} j_i(x, y, t) dy, \quad x = a, b, \quad i = A, B, C.$$

Calculate Darcy-scale interfacial fluxes

$$J_i(x, t) = -\mathcal{D} \frac{\partial C_i}{\partial x}(x, t) + Pe C_{x,i}, \quad x = a, b, \quad i = A, B, C,$$

where $C_i(x, t)$ ($i = A, B$, and C) are computed in step 4.

6. Find the values of $C_{a,i}$ and $C_{b,i}$ ($i = A, B$, and C) that enforce the continuity conditions (23) by solving an optimization problem

$$\operatorname{argmin}_{C_{a,i}, C_{b,i}} \sqrt{\sum_{i=A,B,C} \{[\bar{j}_i(a, t) - J_i(a, t)]^2 + [\bar{j}_i(b, t) - J_i(b, t)]^2\}}.$$

In the simulations reported below we used the Matlab optimization procedure `fmincon` with convergence error of 10^{-9} to solve this problem.

7. Set $t = t + \Delta t$, advance the front's core $x_f(t + \Delta t) = x_f(t) + Pe \Delta t$, and go to step 2.

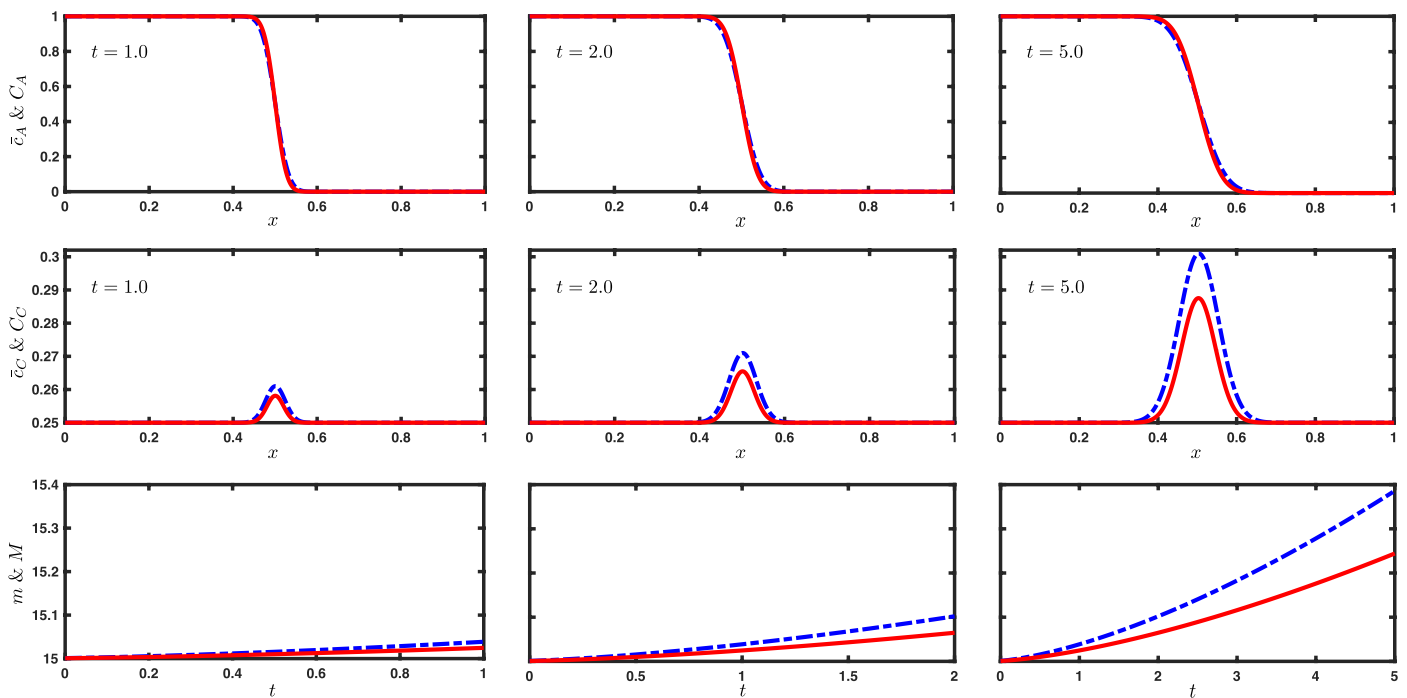


Figure 3. (top and middle) Temporal snapshots, at $t=1.0, 2.0,$ and 5.0 (from left to right), of the averaged pore-scale concentrations $\bar{c}_A(x, t)$ and $\bar{c}_C(x, t)$ (solid line) and their Darcy-scale counterparts $C_A(x, t)$ and $C_C(x, t)$ (dashed line), for Case 1 which satisfies the homogenizability conditions. (bottom) The corresponding total mass of the reaction product in the fracture, computed with the pore-scale (m_C) and Darcy-scale (M_C) models.

4. Simulation Results

We use the Crank-Nicolson scheme with the upwind method for advection terms to solve both the pore-scale problem (13) and Darcy-scale (17) problems. The former was first solved on domain $\Omega = \{\mathbf{x} = (x, y)^T : 0$

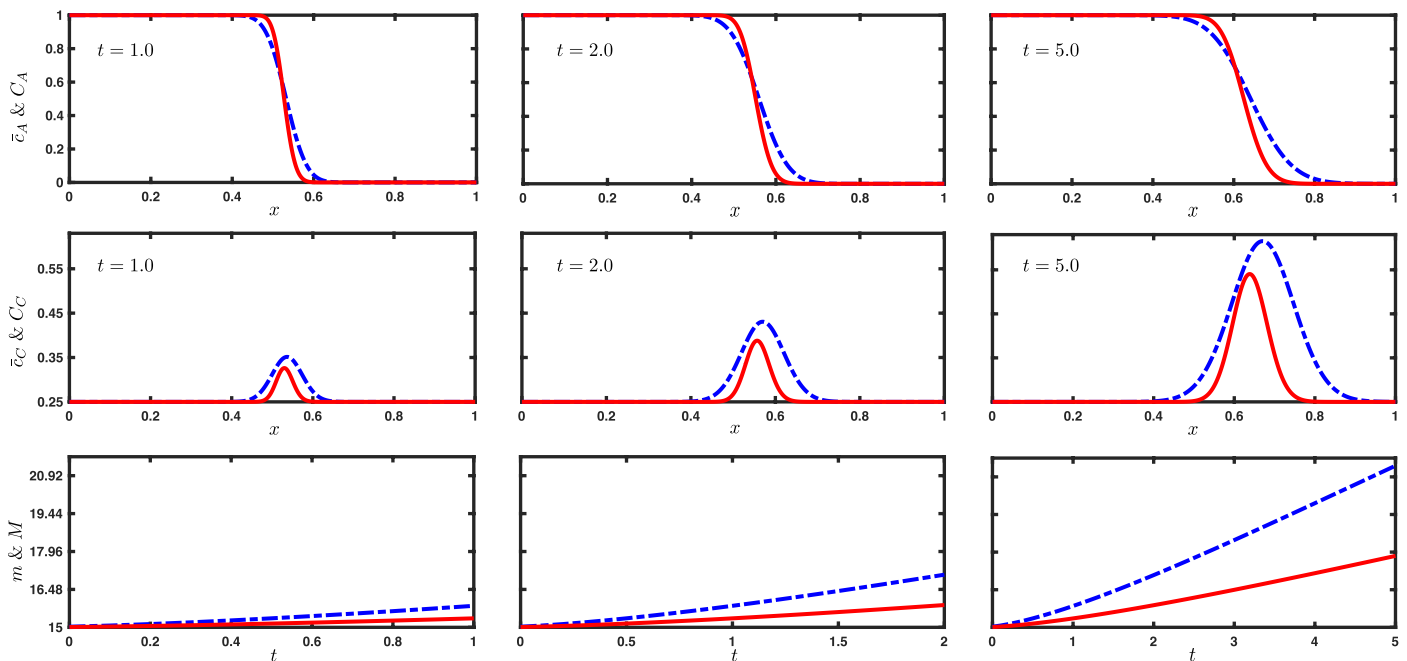


Figure 4. (top and middle) Temporal snapshots, at $t=1.0, 2.0,$ and 5.0 (from left to right), of the averaged pore-scale concentrations $\bar{c}_A(x, t)$ and $\bar{c}_C(x, t)$ (solid line) and their Darcy-scale counterparts $C_A(x, t)$ and $C_C(x, t)$ (dashed line), for Case 2 which violates the homogenizability conditions. (bottom) The corresponding total mass of the reaction product in the fracture, computed with the pore-scale (m_C) and Darcy-scale (M_C) models.

Table 1
Relative Model Errors, $\epsilon_A = 100\% \times \|\bar{c}_A - C_A\|_2 / \|\bar{c}_A\|_2$ and $\epsilon_A^h = 100\% \times \|\bar{c}_A - C_A^h\|_2 / \|\bar{c}_A\|_2$, Introduced by the Use of the Darcy-Scale and Hybrid Simulations, Respectively^a

Model error	t = 1	t = 2	t = 5
Darcy-scale, ϵ_A	4.52	7.82	11.63
Hybrid, ϵ_A^h	0.05	0.11	0.15

^aThe pore-scale result, \bar{c}_A , is treated as “ground-truth.”

$\{x < 1, -\epsilon < y < \epsilon = 0.0625\}$ discretized by a uniform mesh of size $\Delta_x = \Delta_y = 6.25 \times 10^{-5}$ with a time step $\Delta_t = 6.25 \times 10^{-7}$; the latter on domain $\Omega = \{x : 0 < x < 1\}$ discretized by a uniform mesh of size $\Delta_x = 1.25 \times 10^{-3}$ with a time step $\Delta_T = 1.25 \times 10^{-5}$ (Figure 2). This choice of discretization parameters ensures that any disagreement between the pore- and Darcy-scale simulations is solely due to limitations of the Darcy-scale model rather than numerical errors (see Appendix A for detail).

Next, we consider two transport regimes, hereafter referred to as Case 1 and Case 2, which are characterized by different combinations of Pe and Da or, equivalently, $\alpha = -\log_\epsilon Pe$ and $\beta = \log_\epsilon Da$ with $\epsilon = 0.0625$. Case 1 corresponds to $Pe = Da = 0.0625$ which translates into $\alpha = -1$ and $\beta = 1$; this regime satisfies constraints (10) (see Figure 1). Case 2 is characterized by $Pe = 2.0$ and $Da = 64.0$, so that $\alpha = 0.25$ and $\beta = -1.5$; this regime lies outside the homogenizability domain (see Figure 1).

4.1. Impact of Breakdown of the Darcy-Scale Model

For both Cases 1 and 2, we compare the averaged pore-scale concentrations of reactant A and reaction product C with the corresponding Darcy-scale concentrations. The former, $\bar{c}_A(x, t)$ and $\bar{c}_C(x, t)$, are computed with (13) and (20); and the latter, $C_A(x, t)$ and $C_C(x, t)$, with (17). Also compared is the total mass of the reaction product in the fracture, computed with the pore-scale (m_C) and Darcy-scale (M_C) models as

$$m_C(t) = \int_0^1 \bar{c}_C(x, t) dx \quad \text{and} \quad M_C(t) = \int_0^1 C_C(x, t) dx. \quad (24)$$

Figure 3 exhibits these three quantities for Case 1. Since this regime falls within the homogenizability region (Figure 1), one should expect a good agreement between the pore- and Darcy-scale simulations. This is indeed the case. A slight disagreement between the two models’ predictions, which can be quantified in terms of a model error $\mathcal{E}_i = \|\bar{c}_i - C_i\|_2$ ($i = A, B, C$), being approximately of order $\mathcal{O}(\epsilon^2)$, as predicted by the homogenization theory (Boso & Battiato, 2013).

Case 2, which violates the homogenizability conditions, gives rise to a pronounced disagreement between predictions of the pore- and Darcy-scale models (Figure 4). It exemplifies a transport regime in which the advection and diffusion time scales are significantly faster than the reaction time scale. In this regime, the model errors $\mathcal{E}_i > \epsilon$ for all three quantities. By way of example, the relative model error in predictions of the concentration of solute A , introduced by the use of the Darcy-scale simulations, $\epsilon_A = 100\% \times \|\bar{c}_A - C_A\|_2 / \|\bar{c}_A\|_2$, grows with time, reaching $\approx 12\%$ by $t = 5$ (Table 1). This apparent failure of the Darcy-scale model is not only quantitative but also qualitative. While the Darcy-scale model predicts a Gaussian behavior, the averaged pore-scale dynamics is non-Gaussian, as evidenced by the asymmetric, long-tailed concentration profiles.

4.2. Relative Performance of the Hybrid Model

While the transport regime in Case 2 invalidates the reliance of the Darcy-scale model, the use of the pore-scale simulations over the whole transport domain Ω is computationally expensive even for a single fracture

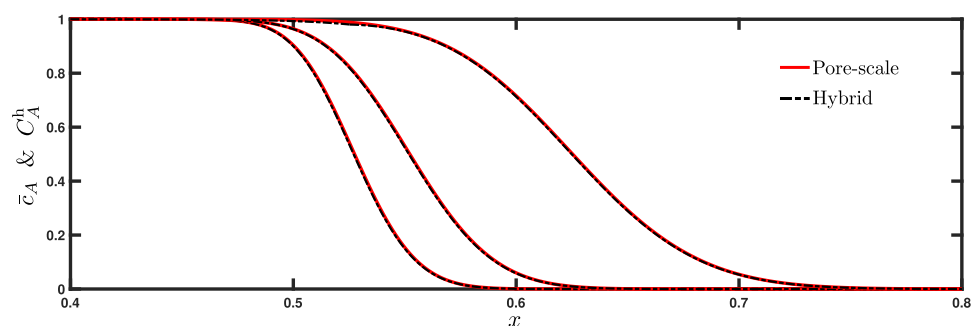


Figure 5. Temporal snapshots, at $t = 1.0, 2.0,$ and 5.0 (from left to right), of the averaged pore-scale concentration $\bar{c}_A(x, t)$ and its counterpart $C_A^h(x, t)$ computed with the hybrid simulations for Case 2.

Table 2
Simulation Time (in Seconds) and Relative Model Error of the Hybrid Simulations, $\epsilon_A^h = 100\% \times \|\bar{c}_A - C_A^h\|_2 / \|\bar{c}_A\|_2$, at $t = 5$ and for Several Sizes $|\mathcal{N}_\delta| = \Delta$ of the Pore-Scale Simulation Domain \mathcal{N}_δ

Δ	0.05	0.10	0.15	0.20	0.30	0.40
ϵ_A^h (%)	0.4301	0.3051	0.2196	0.1573	0.0482	0.00053
Sim. time (s)	391.62	650.71	891.74	1,053.28	1,768.05	2,564.89

(Table A1) and prohibitively so for more complex pore geometries. Instead, we employ the hybrid algorithm described in section 3.2. We start by setting the width of the pore-scale simulation domain to $|\mathcal{N}_\delta| \equiv \Delta = b(t) - a(t) = 0.2$; the Darcy-scale model is solved in the remaining 80% of the simulation domain, $(0, a) \cup (b, 1)$. Visual inspection of Figure 5 demonstrates a close agreement between the exact (pore-scale) solution for the averaged pore-scale concentration $\bar{c}_A(x, t)$ and the hybrid solution $C_A^h(x, t)$. Table 1 further corroborates this observation by collating values of the relative model error $\epsilon_A^h = 100\% \times \|\bar{c}_A - C_A^h\|_2 / \|\bar{c}_A\|_2$ of the hybrid model at different times t . This degree of the hybrid's accuracy is achieved at the fraction of computational cost, yielding a significant reduction relative to that of the pore-scale simulations: 1,053 s for the hybrid model (Table 2) versus 5,975 s for the pore-scale simulations (Table A1). (All computations were carried out on a single-processor laptop.)

The hybrid's accuracy (and computational cost) can be increased by enlarging the region of the computational domain, $\mathcal{N}_\delta(t)$, wherein the pore-scale simulations are performed. Alternatively, the hybrid's computational cost can be reduced by decreasing the size of $\mathcal{N}_\delta(t)$, at the cost of reducing the hybrid's accuracy (Table 2). Even the smallest size of \mathcal{N}_δ reported in Table 2, $|\mathcal{N}_\delta(t)| = \Delta = 0.05$, yields an acceptable relative model error ($\epsilon_A^h = 0.43\%$). The increase in the hybrid's accuracy and computational cost with Δ is to be expected, since the accurate and expensive pore-scale simulations are carried out over the progressively larger domain \mathcal{N}_δ . Refining the mesh size and time step of the Darcy-scale component of the hybrid is relatively inexpensive but does not yield a significant improvement in the relative model error (Table A2).

5. Summary and Conclusions

We developed a hybrid model of propagation of reactive fronts. These fronts involve an irreversible homogeneous reaction $A + B \rightarrow C$ and are highly localized due to an initial distribution of reactants A and B . A set of numerical experiments for multicomponent reactive flow in a horizontal open fracture is performed to demonstrate that dynamic reactive fronts might not be amenable to Darcy-scale modeling. Our hybrid algorithm couples the pore-scale model in the vicinity of a moving reaction front with the Darcy-scale model elsewhere in the fracture.

Our study leads to the following major conclusions.

- Necessary conditions for the breakdown of Darcy-scale models of dynamic reactive fronts are presented as a phase diagram in the space of the Péclet (Pe) and Damköhler (Da) numbers. Our simulations provide an example of the failure of a Darcy-scale model whose parameters fall outside the homogenizability region in this diagram.
- The observed failure of the Darcy-scale model of reaction fronts in an open fracture is not only quantitative but also qualitative. While the Darcy-scale model predicts a Gaussian behavior, the true dynamics is non-Gaussian, as evidenced by the asymmetric, long-tailed concentration profiles.
- The representational accuracy of our hybrid algorithm is comparable to that of high-fidelity pore-scale simulations, but at the fraction of computational cost.
- The hybrid formulation does not require any additional parameters beyond those used in macroscopic or microscopic models.
- The hybrid formulation for the moving dynamic fronts suggests its high adaptability to a wide variety of problems and different numerical schemes.

In follow-up studies, we will employ our hybrid algorithm to model dynamic reaction fronts, which propagate in porous media and involve two-phase incompressible flow.

Appendix A: Verification of Numerical Simulations

To ensure that our numerical solutions of the pore-scale (13) and Darcy-scale (17) models are not significantly affected by their space-time discretization, we progressively refine the mesh size and time step. Starting with $\Delta_x = \Delta_y = 10^{-3}$ and $\Delta_t = 10^{-5}$, the space-time discretization of (13) is refined according to

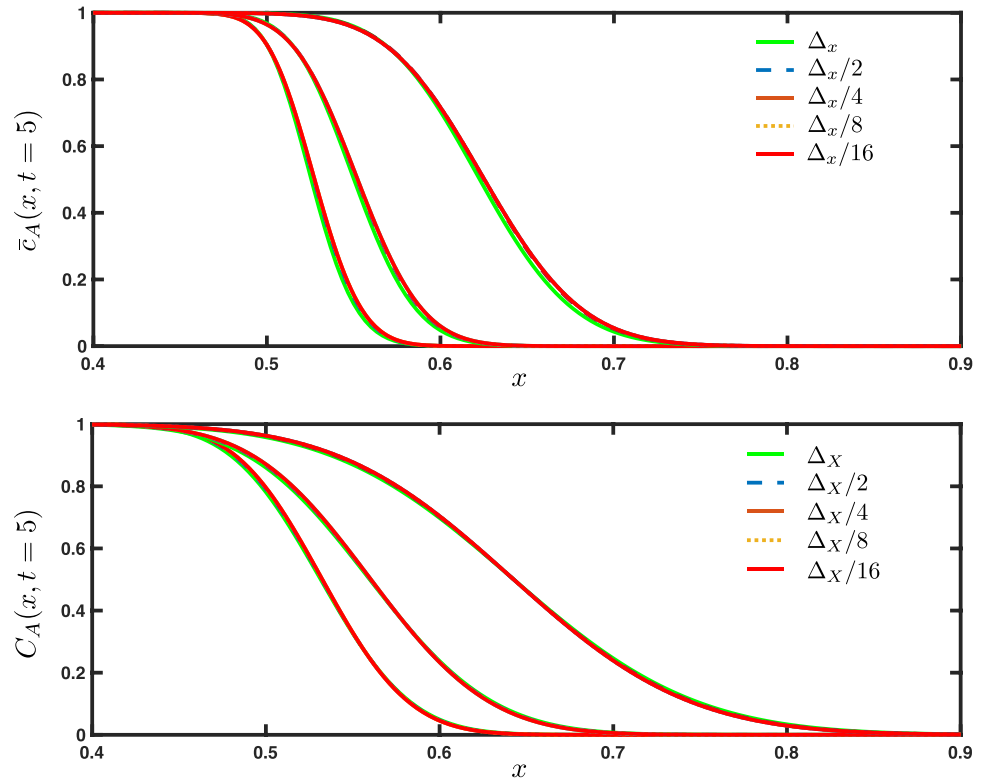


Figure A1. Spatial profiles of (top) averaged pore-scale concentration $\bar{c}_A(x, t)$ and (bottom) Darcy-scale concentration $C_A(x, t)$ at times $t = 1, 2$, and 5 (from left to right) for the transport regime characterized by $\alpha = 1/4$ and $\beta = -3/2$. The former is computed with (13) and (20), the latter with (17). Both use the progressively finer time-space discretizations.

$\Delta_x/2^k = \Delta_y/2^k$ and $\Delta_t/2^k$ with $k = 0, 1, \dots$. Likewise, starting with $\Delta_X = 10^{-2}$ and $\Delta_T = 10^{-4}$, the space-time discretization of (17) is refined according to $\Delta_X/2^k$ and $\Delta_T/2^k$ with $k = 0, 1, \dots$. Results of this mesh refinement

are reported in Figure A1 for the averaged pore-scale concentration $\bar{c}_A(x, \cdot)$ computed with (13) and (20) and for the Darcy-scale concentration $C_A(x, \cdot)$ computed with (17). The refinement beyond $k = 2$ shows no visual improvement. (Although not shown here, the concentrations of species B and C exhibit an identical behavior.)

This assessment is made more quantitative by defining a relative discretization error

$$\mathcal{E}_k(f) = \frac{\|f_k - f_{k+1}\|_2}{\|f_{k+1}\|_2}, \quad k = 0, 1, 2, \dots$$

where $f_k = \bar{c}_A(\Delta_x/2^k = \Delta_y/2^k, \Delta_t/2^k)$ or $f_k = C_A(\Delta_X/2^k, \Delta_T/2^k)$. Table A1 demonstrates that the discretization error of 10^{-4} is achieved with the refinement levels of $k = 4$ for the pore-scale simulations and $k = 3$ for the Darcy-scale simulations. Further refinement does not substantially improve the discretization error, but considerably increases the simulation time. These values of the discretization parameters are used in all the simulations reported in this study.

Finally, we explore benefits of refining the space-time discretization of the Darcy-scale component of the hybrid, $\{\Delta_X/2^k, \Delta_T/2^k\}$, while keeping the discretization of the pore-scale component fixed at $\{\Delta_x/2^4, \Delta_y/2^4, \Delta_t/2^4\}$. Such refinement does not improve the hybrid's accuracy, quantified in terms of the relative model error $\epsilon_A^h = 100\% \times \|\bar{c}_A - C_A^h\|_2 / \|\bar{c}_A\|_2$ for the hybrid model (Table A2). Hence, going

Table A1

Relative Discretization Errors, \mathcal{E}_k , and Simulation Times, in Seconds, for the Averaged Pore-Scale (\bar{c}_A) and Darcy-Scale (C_A) Estimates of the Concentration of Species A at Time $t = 1.0$ on the Meshes and Time Steps Refined by the Factor of 2^k

Refinement level, k	Relative error, $\mathcal{E}_k(f) \times 10^{-3}$		Simulation time (s)	
	$f = \bar{c}_A$	$f = C_A$	\bar{c}_A	C_A
0	5.458	8.20763	57.19	2.24
1	2.542	1.31274	162.92	7.53
2	0.503	0.54580	546.83	20.69
3	0.285	0.05137	1,760.09	69.48
4	0.09215	0.05011	5,975.24	247.98
5	0.08973	–	15,627.45	–

Table A2

Relative Model Error of the Hybrid Simulations, ϵ_A^h , at $t = 1.0$ and for Several Levels of Refinement, k , of the Darcy-Scale Component

Refinement level, k	3	4	5
ϵ_A^h (%)	0.0529	0.0517	0.0503

Note. The discretization of the pore-scale component is fixed at $\Delta_x/2^4, \Delta_y/2^4, \Delta_t/2^4$.

above the refinement level $k = 3$ for the Darcy-scale component of the hybrid only increases the computational time.

Acknowledgments

The data used are listed in the references and tables. This work was supported in part by the National Science Foundation under grant CBET-1563614.

References

- Alexander, F. J., Garcia, A. L., & Tartakovsky, D. M. (2002). Algorithm refinement for stochastic partial differential equations: 1. Linear diffusion. *Journal of Computational Physics*, *182*, 47–66.
- Alexander, F. J., Garcia, A. L., & Tartakovsky, D. M. (2005a). Algorithm refinement for stochastic partial differential equations: II. Correlated systems. *Journal of Computational Physics*, *207*(2), 769–787.
- Alexander, F. J., Garcia, A. L., & Tartakovsky, D. M. (2005b). Noise in algorithm refinement methods. *Computing in Science & Engineering*, *7*(3), 32–38.
- Balhoff, M. T., Thomas, S. G., & Wheeler, M. F. (2008). Mortar coupling and upscaling of pore-scale models. *Computers & Geosciences*, *12*(1), 15–27.
- Battiato, I., & Tartakovsky, D. M. (2011). Applicability regimes for macroscopic models of reactive transport in porous media. *Journal of Contaminant Hydrology*, *120–121*, 18–26. <https://doi.org/10.1016/j.jconhyd.2010.05.005>
- Battiato, I., Tartakovsky, D. M., Tartakovsky, A. M., & Scheibe, T. (2009). On breakdown of macroscopic models of mixing-controlled heterogeneous reactions in porous media. *Advances in Water Resources*, *32*, 1664–1673. <https://doi.org/10.1016/j.advwatres.2009.08.008>
- Battiato, I., Tartakovsky, D. M., Tartakovsky, A. M., & Scheibe, T. D. (2011). Hybrid models of reactive transport in porous and fractured media. *Advances in Water Resources*, *34*(9), 1140–1150.
- Boso, F., & Battiato, I. (2013). Homogenizability conditions for multicomponent reactive transport. *Advances in Water Resources*, *62*, 254–265. <https://doi.org/10.1016/j.advwatres.2013.07.014>
- Coveney, P. V., & Fowler, P. W. (2005). Modelling biological complexity: A physical scientist's perspective. *Journal of the Royal Society Interface*, *2*(4), 267–280.
- De Wit, A. (2004). Miscible density fingering of chemical fronts in porous media: Nonlinear simulations. *Physics of Fluids*, *16*(1), 163–175.
- Fernandez, J., & Homsy, G. M. (2003). Viscous fingering with chemical reaction: Effect of in-situ production of surfactants. *Journal of Fluid Mechanics*, *480*, 267–281.
- Gálfi, L., & Rácz, Z. (1988). Properties of the reaction front in an $A+B \rightarrow C$ type reaction-diffusion process. *Physical Review A*, *38*(6), 3151–3154.
- Johnson, J. N., Tang, P. K., & Forest, C. A. (1985). Shock-wave initiation of heterogeneous reactive solids. *Journal of Applied Physics*, *57*(9), 4323–4334.
- Roubinet, D., & Tartakovsky, D. M. (2013). Hybrid modeling of heterogeneous geochemical reactions in fractured porous media. *Water Resources Research*, *49*, 7945–7956. <https://doi.org/10.1002/2013WR013999>
- Tang, Y., Valocchi, A. J., & Werth, C. J. (2015). A hybrid pore-scale and continuum-scale model for solute diffusion, reaction, and biofilm development in porous media. *Water Resources Research*, *51*, 1846–1859. <https://doi.org/10.1002/2014WR016322>
- Tartakovsky, A. M., Tartakovsky, D. M., Scheibe, T. D., & Meakin, P. (2008). Hybrid simulations of reaction-diffusion systems in porous media. *SIAM Journal on Scientific Computing*, *30*(6), 2799–2816.
- Taverniers, S., Alexander, F. J., & Tartakovsky, D. M. (2014). Noise propagation in hybrid models of nonlinear systems: The Ginzburg-Landau equation. *Journal of Computational Physics*, *262*, 313–324. <https://doi.org/10.1016/j.jcp.2014.01.015>
- Tomin, P., & Lunati, I. (2013). Hybrid multiscale finite volume method for two-phase flow in porous media. *Journal of Computational Physics*, *250*, 293–307.